Nuclear Instruments and Methods in Physics Research A240 (1985) 410–428
North-Holland, Amsterdam

THE UTAH FLY'S EYE DETECTOR

R.M. BALTRUSAITIS, R. CADY *, G.L. CASSIDAY, R. COOPER, J.W. ELBERT, P.R. GERHARDY, S. KO, E.C. LOH, M. SALAMON **, D STECK and P. SOKOLSKY

Department of Physics, University of Utah, Salt Lake City, UT 84112, USA

Received 5 December 1984 and in revised form 13 May 1985

We report the details of the design, operation and performance of the University of Utah Fly's Eye detector which was built to record the passage of ultra-high energy cosmic rays through the atmosphere via atmospheric fluorescence. Emphasized in the presentation are (1) light production by charged particles in the atmosphere, (2) kinematics of an EAS as seen by the Fly's Eye, (3) signal to noise considerations and its impact on detector design, (4) details of detector hardware and software, (5) detector calibration, (6) techniques employed in measurement of shower longitudinal development profiles and primary particle energy, and (7) assessment of detector performance by a comparison of Monte Carlo and real data distributions.

1. Introduction

The University of Utah has constructed a large high energy physics/astrophysics observatory on top of Little Granite Mountain, Dugway, Utah, approximately 160 km south-west of Salt Lake City, Utah. The observatory was designed to detect the passage of extensive air showers (EAS) through the atmosphere by means of the nitrogen fluorescence light given off after excitation by the relativistic charged particles in the shower. Experiments being carried out with the detector include: (1) a direct measurment of the proton–air cross section at $s^{1/2} = 30$ TeV, (2) an analysis of the primary cosmic ray spectrum in the energy range 0.01–100 EeV (10^{18} eV) with emphasis on the 3 K blackbody cutoff region near 60 EeV, (3) an extraction of the composition of high energy cosmic ray primaries, (4) a search for anisotropies in arrival directions, (5) a search for deeply penetrating showers indicative of primary neutrinos, heavy lepton production or quark matter in the primary flux, and (6) a search for sources of γ-rays near 1 PeV (10^{15} eV).

Previous experiments with EAS have involved ground-based particle detector arrays in which the properties of the showers have been inferred from a sample of the secondaries taken at a few locations along the shower front at a single atmospheric depth [1], or Cherenkov detector arrays which employ fast timing measurements of samples of the shower-generated Cherenkov wavefront to obtain an integral history of the shower [2]. In each of these cases, observations are limited to small areas and low event rates for high energy showers as well as poor (if any) resolution of shower longitudinal development. The Fly's Eye detector was designed and built to overcome these two experimental deficiencies.

The attractiveness of the Fly's Eye technique is, unfortunately, tarnished somewhat by the low duty cycle (5–10%) imposed by the constraint of operating a 2π field of view optical detector only on clear, moonless nights. However, it was hoped that this effect could be more than offset by detecting events at distances of, perhaps, 20 km or more away from the observatory giving rise to an incredibly large fiducial area on the order of 10^3–10^4 km^2 sr. The experimental goals to be carried out by the Fly's Eye experiment depend crucially upon its ability to not only "see" the highest energy cosmic rays at such remote distances but also to see each event with enough clarity such that the energy of the primary cosmic ray can be ascertained in a fairly model independent way. Furthermore, it was anticipated that shower profiles of a subclass of events in a more restrictive energy range could be well enough resolved that information on primary composition and proton–air total cross section could be obtained. In the following sections of this paper, we present design and operational details of the Fly's Eye detector along with those results so far obtained which illustrate how far this novel experimental technique has evolved in pursuit of the abovementioned goals.

1.1. Brief description of the Fly's Eye

The Fly's Eye observatory (fig. 1) consists of two experimental stations (Fly's Eye I and Fly's Eye II) separated by 3.3 km. Fly's Eye I consists of 67 62-inch front aluminized spherical section mirrors, associated Winston light collectors, photomultiplier tubes (PMT) and data acquisition electronics. The Winston light collectors and PMTs are hexagonally packed in groups of either 12 or 14 light sensing "eyes" mounted in the focal plane of each mirror. A motorized shutter system keeps the eyes both light tight and weather proof during the day and permits exposure to the sky at night. Each mirror unit and associated light sensing cluster is housed in a single, motorized corrugated steel pipe about 2.13 m long and 2.44 m in diameter. The units are turned down with mirror and open end facing the ground during the day (to protect cluster and mirror from light and weather), and turned up at night to a predetermined position so that each "eye" observes a designated angular region of the sky. In all, there are 880 eyes at Fly's Eye I, which completely image the entire night sky. The projection of each hexagonal "eye" onto the celestial sphere resembles the compound eye of an insect; hence the name, Fly's Eye. Shown in fig. 2 is a picture of a single mirror housing unit and associated optical cluster. Fly's Eye II is a smaller array of identical units, 8 in all, with 120 total eyes. Fly's Eye II observes roughly one azimuthal quadrant of the night sky with elevation angles ranging between 2° and 38° above the horizon.

Signals from each PMT are cabled to a central trailer which houses all data acquisition electronics, computers and living quarters. Each PMT is operated in a grounded cathode configuration followed by a transconductance amplifier to convert the PMT anode current to a voltage. The PMTs are serviced by a signal cable, HV cable, and a 4-conductor cable carrying a test strobe input to the pre-amp, ±15 V supply and ground. All cables are housed in grounded steel conduit to protect them from weather, lightning, and certain undesired life forms which populate remote desert areas.

Briefly, the central electronics consists of triggering and pulse integral measuring circuitry, arrival time latches, digitization and control electronics. The electronics operates under computer control and extensive

Fig. 1. Aerial view of the Fly's Eye I detector. The detector is located on top of Little Granite Mountain, elevation 860 g cm^{-2}, Dugway, Utah.

---

[*] Present address: Department of Physics, University of Hawaii, Honolulu, HI 96822, USA.

[**] Present address: Department of Physics, University of California, Berkeley, CA 94720

0168-9002/85/$03.30 © Elsevier Science Publishers B.V. (North-Holland Physics Publishing Division)

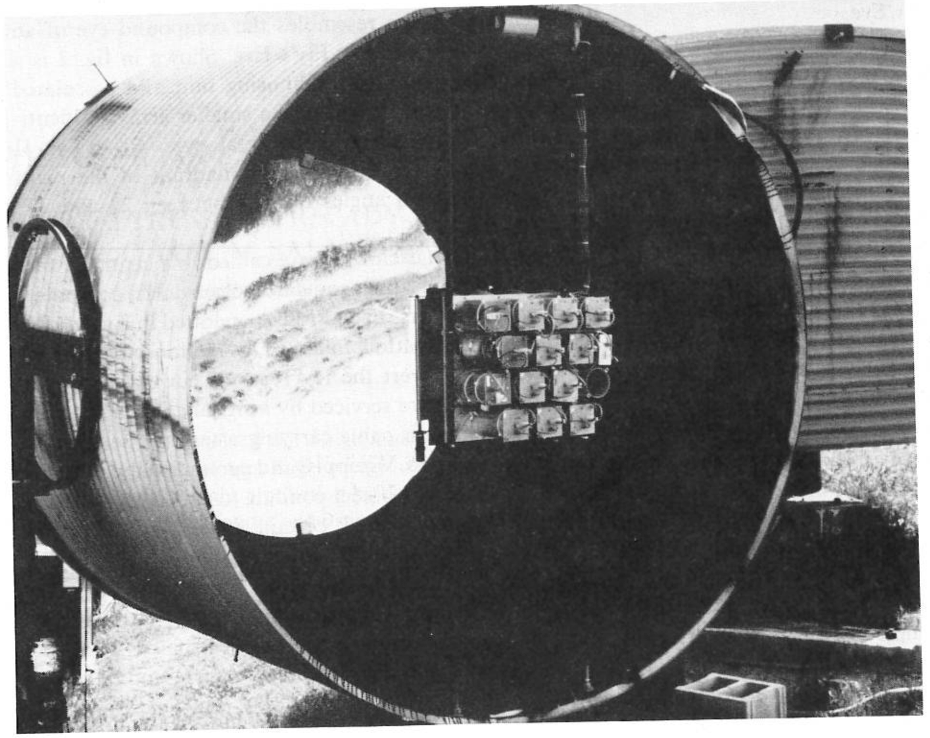

Fig. 2. Single mirror unit. A 62 in. mirror is housed in a large 2.13 m×2.44 m motorized, corrugated steel pipe. A cluster of 14 Winston cone light collectors, PMTs and associated preamps is mounted in the mirror's focal plane. An optical pulser unit is positioned just inside the corrugated housing above the PMT cluster.

sofware exists for circuit diagnostics, data acquisition, pattern recognition and system control.

On clear, moonless nights an operator at each site activates the detector which records the pulse integral and arrival times generated by each visible EAS as it progresses across the celestial sphere. Whenever Fly's Eye I triggers, it sends an infrared flash of light toward Fly's Eye II which, if also triggered by the "simultaneous" observation of something in the night sky, records its own pulse integral and arrival times. EAS track geometry may then be reconstructed either from hit patterns and timing by a single Fly's Eye detector or by stereoscopic viewing and relative timing by both Fly's Eyes. Once the geometry of an EAS track is determined, shower longitudinal development profiles and total shower energy can be obtained on an event by event basis from measured pulse integrals after suitable correction for light attenuation and Cherenkov light contamination.

2. EAS light production mechanisms

The fundamental problem of detecting an EAS via air fluorescence can be best imagined as follows: Consider an apparent blue (actually near uv), 5-W light bulb streaking through the sky at the speed of light against a continuous backdrop of starlight, atmospheric airglow and man-made light pollution. In addition, sporadic sources of light such as lightning, auroras, airplane and smokestack strobe lights (visible for hundreds of miles) create a certian visual havoc. The task of the Fly's Eye is to pick out this faint, but fast signal from the ambient background noise.

Four basic mechanisms contribute to the generation of the light signal seen by the Fly's Eye detector: (i) fluorescence, (ii) direct Cherenkov light, (iii) Rayleigh-scattered Cherenkov light, and (iv) Mie-scattered Cherenkov light. Of these, fluorescence is the one which relates most directly to the numbers of charged particles in an EAS seen by any particular PMT. Fortunately, it is the major light contributor for showers seen both at altitudes and impact parameters exceeding 2 km or so relative to the detector.

2.1. *Atmospheric fluorescence*

Most of the energy of a primary cosmic ray is dissipated in the atmosphere by the ionization and excitation of air molecules. Nearly all of the optical fluorescence comes from the 2P band system of molecular nitrogen and the 1N band system of the N_2^+ molecular ion [3–5]. The measured fluorescence spectrum is shown in fig. 3a. It is normalized to 4.32 γ/MeV at 337.1 nm. We use an EMI 9861B PMT with a super S-11 response which has a fairly uniform quantum efficiency over the spectral range 310–440 nm (the peak quantum efficiency is $\varepsilon \simeq 0.21$ at $\lambda \simeq 360$ nm). The resultant fluorescent yield as a function of altitude integrated over our spectral response is shown in fig. 3b. It is mildly altitude and temperature dependent. The mildness of the altitude dependency is the fortuitous result of two competing effects: (1) the number of excitations per unit path length is proportional to pressure while (2) the fluorescence efficiency is inversely proportional to pressure due to the increasing probability of collisional de-excitation. The angular distribution of the fluorescent light can roughly be approximated by

$$\frac{\mathrm{d}^2 N}{\mathrm{d}l\,\mathrm{d}\Omega} \cong \frac{N_\gamma N_\mathrm{e}}{4\pi}, \qquad (1)$$

where N_γ is the fluorecent yield in photons/electron/m and N_e is the number of electrons in the EAS generating the light. The resultant light yield corresponds to a scintillation efficiency of only 0.5%. However, the poor efficiency is compensated for by the overwhelming amount of energy being dissipated by a 100 EeV EAS – more than 1 J in 30 μs!

2.2. *Cherenkov light*

Electrons in an EAS (which typically overwhelm all other charged particles by about a factor of 10^2) generate a prodigious amount of Cherenkov light which is primarily beamed in the forward direction [6–8]. The amount of Cherenkov light at any point along the shower front depends upon the previous history of the shower, and thus is not strictly proportional to local shower size as is the case for scintillation light. Unfortunately, directly-beamed Cherenkov light dominates the light seen by the Fly's Eye detector at emission angles relative to the EAS axis of less than 25° which makes the inference of shower size difficult for early stages of development. Moreover, as the Cherenkov component builds up with the propagating shower front, the resultant intense beam can generate enough scattered light at low altitudes such that it competes with the locally produced scintillation light from the rapidly-dying shower. Even so, scattered Cherenkov light usually constitutes in worst case situations no more than about 30% of the total light seen whereas the directly-beamed Cherenkov light at small angles may swamp scintillation light by a factor of 10^2. These considerations severely limit the accuracy of shower size measurement for those EAS which strike within a kilometer or so of the Fly's Eye detector since much of the developing shower can only be observed at emission angles less than 25° under such circumstances. The Cherenkov problem obviously becomes less of a nuisance for the more remotely-viewed showers. An exact calculation of the Cherenkov light signal (both direct as well as scattered) is quite complicated and must be carried out numerically. Here, we present simplified calculations whose results are accurate to within roughly 10%.

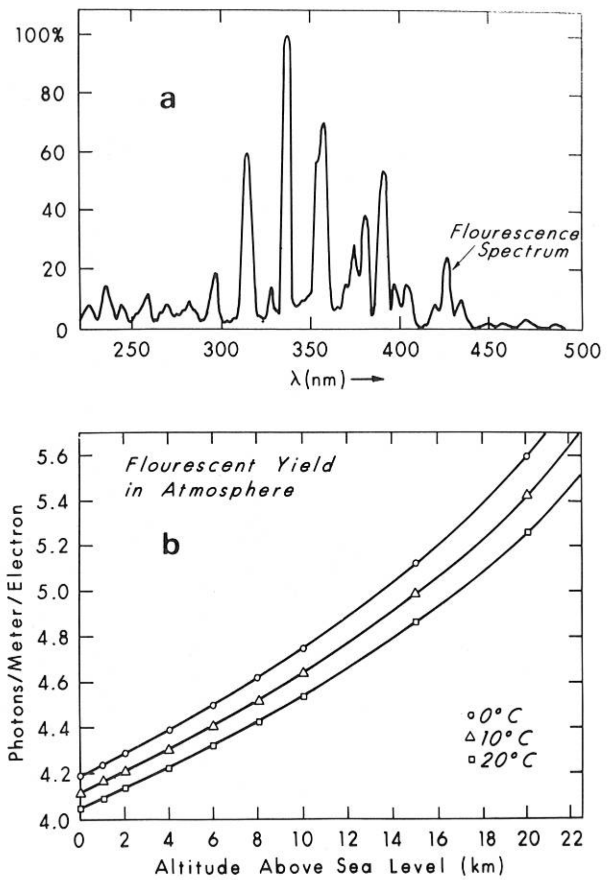

Fig. 3. (a) Atmospheric fluorescence spectrum emanating mostly from the 2P band of molecular nitrogen and the 1N band of the N_2^+ molecular ion. (b) Fluorescent yield (equivalent 360 nm photons/(electron m)) as a function of altitude (km).

A single relativistic particle in air produces N_γ Cherenkov photons per unit length

$$\frac{\mathrm{d}N_\gamma}{\mathrm{d}l} = 2\pi\alpha \int \left(1 - \frac{1}{\beta^2 n^2}\right) \mathrm{d}\frac{\nu}{c}, \qquad (2)$$

where ν is the frequency of the radiation and n is the index of refraction of air. Practical limits for the range of integration are determined by the spectral response of the viewing optical system and the transmission properties of the atmosphere. Since $n \simeq 1$, the above integrand can be approximated as

$$\begin{aligned} 1 - (\beta n)^{-2} &= 1 - \left(1 - \frac{m^2 c^4}{E^2}\right)^{-1} (1+\delta)^{-2} \\ &\approx 2\delta - \frac{m^2 c^4}{E^2}, \qquad (3) \end{aligned}$$

where $\delta = n - 1$. The electrons in an air shower have a distribution $f(E)$ defined such that

$$F(E) = \int_E^\infty f(\tilde{E})\,\mathrm{d}\tilde{E} \qquad (4)$$

is the fraction of electrons in the shower with energies greater than E. The rate of Cherenkov photon generation by N_e electrons distributed according to $f(E)$ is then

$$\frac{\mathrm{d}N_\gamma}{\mathrm{d}l} = \frac{2\pi\alpha}{c} N_e \int \mathrm{d}\nu \int_{E_t}^{\infty} f(E)\left(2\delta - \frac{m^2c^4}{E^2}\right)\mathrm{d}E, \qquad (5)$$

where E_t is the Cherenkov photon production threshold energy for a relativistic electron in air given by

$$E_t = mc^2/\sqrt{2\delta}\,. \qquad (6)$$

For an isothermal atmosphere approximation, δ is approximately

$$\delta = \delta_0 e^{-h/H_0}, \qquad (7)$$

where δ_0 is the value of δ at the local surface. At Fly's Eye altitude (860 g cm^{-2}) $\delta_0 = 2.4 \times 10^{-4}$ and the atmospheric scale height is $H_0 \simeq 7.3$ km.

The distribution $F(E)$ has been evaluated by Hillas [9] and found to be mildly dependent on shower age. We use 1.0 for the age in evaluating $F(E)$ since the age of most particles observed in an EAS are not too different from that value. Thus, we find

$$F(E) = \frac{34.8}{(40.4 + E)(1 + 10^{-4}E)^2} \qquad (8)$$

(with E in MeV). Therefore, to within a few percent, we obtain

$$\int_{E_t}^{\infty} f(E)\left(2\delta - \frac{m^2c^4}{E^2}\right)\mathrm{d}E = 2\delta F(1.57E_t), \qquad (9)$$

Given that the bandwidth of Fly's Eye spectral response is roughly 250 nm we estimate

$$\frac{\mathrm{d}N_\gamma}{\mathrm{d}l} \simeq 33 N_e F(1.57E_t)\exp(-h/H_0) \qquad (10)$$

Cherenkov photons/m produced along the shower's trajectory.

The angular distribution of scattered Cherenkov light has been calculated most recently by Elbert et al. [10], and is due primarily to the angular distributions of electrons in the shower. For the most important angular region ($\theta < 30°$) under consideration here for direct Cherenkov light, $\mathrm{d}N/\mathrm{d}\theta$ is an exponential whose characteristic angle θ_0 depends on Cherenkov threshold and is given by

$$\theta_0 \approx 0.83 E_t^{-0.67}. \qquad (11)$$

The resultant Cherenkov light production is then

$$\frac{\mathrm{d}^2N_\gamma}{\mathrm{d}l\,\mathrm{d}\Omega} = \frac{\mathrm{d}N_\gamma}{\mathrm{d}l}\,\frac{e^{-\theta/\theta_0}}{2\pi\sin\theta}. \qquad (12)$$

2.3. Rayleigh scattering

Light signals seen by the Fly's Eye are both enhanced as well as diminished by two mechanisms, Rayleigh and Mie scattering. Light scattering removes light from a beam propagating towards the Fly's Eye from an EAS source while it enhances the source brightness by scattering the accompanying Cherenkov light beam toward the Fly's Eye. Rayleigh scattering (scattering of light from air molecules) is proportional to $\rho\,\mathrm{d}l/\lambda^4$, where ρ is the local air density and λ is the wavelength of the scattered light. At sea level the Rayleigh scattering length [11] is 23 km at 400 nm which corresponds to a mean free path of $x_R = 2974$ g cm^{-2}. Thus, the amount of light Rayleigh scattered from a beam of N_γ photons is

$$\frac{\mathrm{d}N_\gamma}{\mathrm{d}l} = -\rho\frac{N_\gamma}{x_R}\left(\frac{400}{\lambda}\right)^4. \qquad (13)$$

For an isothermal atmosphere

$$\rho = \rho_0 e^{-h/H_0}, \qquad (14)$$

where $\rho_0 = 0.00107$ g cm^{-2} at 0°C at Fly's Eye altitude.

For the purposes of estimating the amount of Cherenkov light scattered out of the Cherenkov beam accompanying the EAS toward the Fly's Eye at an angle θ within an solid angle $\mathrm{d}\Omega$ we have

$$\frac{\mathrm{d}^2N_\gamma}{\mathrm{d}l\,\mathrm{d}\Omega} = \frac{\mathrm{d}N_\gamma}{\mathrm{d}l}\,\frac{3}{16\pi}(1 + \cos^2\theta). \qquad (15)$$

2.4. Mie scattering

Mie scattering is scattering of light by small, particulate particles (aerosols) whose size is comparable to the wavelength of light. It constitutes only a minor correction to the light received by the Fly's Eye detector. According to the observations of Flowers et al. [11], the Dugway, Utah location of the Fly's Eye is in one of the most favorable, clean air locations of the country where aerosol contamination is minimal. Also, the Fly's Eye sits on a mountain top at high elevation which is also advantageous, since aerosol concentrations fall rapidly with altitude.

Estimates of Mie scattering are based upon the model of Elterman [12]. Here, for the sake of simplification, Mie scattering is assumed to fall off exponentially with altitude. The amount of light Mie scattered from a beam of N_γ photons is approximately

$$\frac{\mathrm{d}N_\gamma}{\mathrm{d}l} = -\frac{N_\gamma}{L_M} e^{-h/H_M}, \qquad (16)$$

where $H_M = 1.2$ km is the scale height, and $L_M = 14$ km, a typical Mie scattering mean free path at 360 nm. The angular distribution is strongly peaked in the forward direction although not so strong as that of the direct Cherenkov light. An approximate angular form which works extremely well for angles in the range 5°–60° is given by

$$\frac{\mathrm{d}^2N}{\mathrm{d}l\,\mathrm{d}\Omega} \simeq \frac{\mathrm{d}N_\gamma}{\mathrm{d}l}\,0.80\,e^{-\theta/\theta_M}, \qquad (17)$$

where $\theta_M \simeq 26.7°$.

2.5. Attenuation

Measured light yields at a receiver must be corrected for beam attenuation losses due to Rayleigh and Mie scattering. Let the location of source and receiver be x_1 and x_2 given in atmospheric slant depths, i.e.,

$$x = x_0\,e^{-h/H_0}\sec\theta, \qquad (18)$$

where $x_0 = 860$ g cm^{-2}, the vertical "depth" of the Fly's Eye detector. The Rayleigh transmission factor, T_R, or that fraction of photons not Rayleigh scattered from the beam can easily be calculated from eq. (13).

Since $\rho\,\mathrm{d}l = \mathrm{d}x$ we have

$$T_R = \exp\left\{-\left(\frac{|x_1 - x_2|}{x_R}\right)\left(\frac{400\ \mathrm{nm}}{\lambda}\right)^4\right\}. \qquad (19)$$

For Mie scattering we obtain a corresponding transmission factor, in this case relating the two heights of source and receiver h_1 and h_2 by integrating eq. (16) ($h_1 > h_2$):

$$T_M = \exp\left\{\left(\exp\left(-\frac{h_1}{H_M}\right) - \exp\left(-\frac{h_2}{H_M}\right)\right) H_M \sec\theta / L_M\right\}. \qquad (20)$$

The overall transmission factor for a light beam propagating from source to receiver is thus

$$T = T_R T_M. \qquad (21)$$

2.6. Total signal strength

Shown in fig. 4 are relative photoelectron yields generated by a shower of size N_e via the various light generating mechanisms discussed above. The curves labelled Sc, C, R and M refer to yields generated by scintillation, direct Cherenkov, Rayleigh and Mie scattered Cherenkov light. Scattered light is always inconsequential during the early developmental stages of a shower. Hence, the initial size of the shower can be deduced by assuming that the received light is all direct Cherenkov and scintillation light. This permits an accurate estimate of the Cherenkov beam build-up which is necessary for calculating those scattering corrections which must be applied at subsequent stages of shower development. Upon applying those corrections to the total yield, the residual yield due to fluorescence can be used to directly infer the size of the EAS as a function of depth.

2.7. Noise

Essential noise mechanisms limiting detector sensitivity include night sky radiation which is produced by

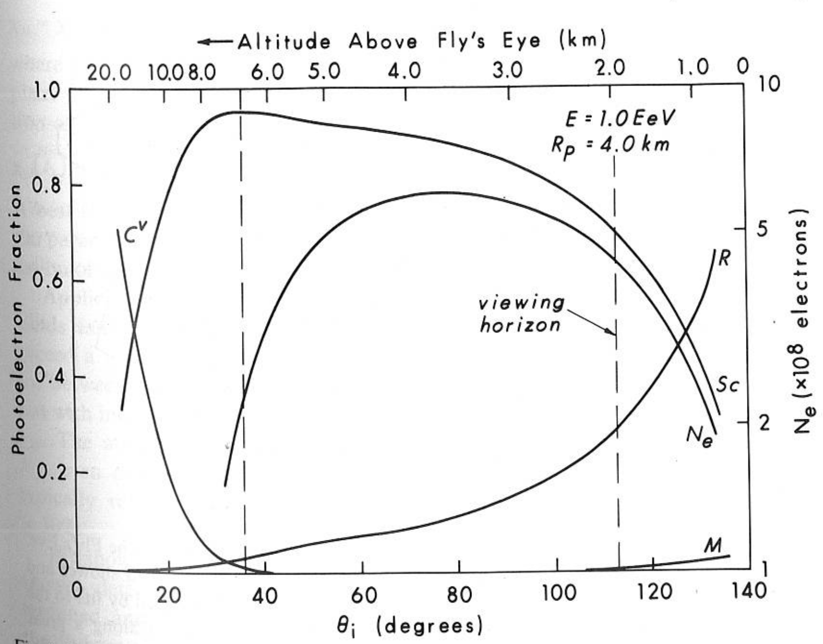

Fig. 4. Relative photoelectron yields produced via all light generating mechanisms as a function of altitude above the Fly's Eye (upper scale) and EAS emission angle θ (lower scale). Sc is for scintillation light, C for direct Cherenkov, R for Rayleigh scattered and M for Mie-scattered Cherenkov light. The curve labelled N_e is the actual shower profile whose size is on the right.

scattered starlight, diffuse radiation of the galaxy, light from subthreshold stars, light from other galaxies and intergalactic matter, sunlight scattered by interplanetary matter and light produced by photochemical processes in the earth's ionosphere [13,14]. These sources of light induce a dc signal in any phototube aimed at the night sky and fluctuations in this dc signal constitute the noise. An additional important source of noise is caused by Cherenkov light generated by low energy cosmic rays ($E < 1$ PeV) which strike the detector head-on resulting in a "rain" of sharp, fast pulses. In fact, this latter noise source can be treated as a real signal if one is interested in the physics appropriate to such low energy cosmic rays. Other noise sources, such as airplane and smokestack strobes, meteors, or fireflies, though an incredible nuisance, do not constitute a fundamental problem.

In the relevant spectral region covered by our PMT response, the night sky background averages about a fourth magnitude per square degree [15,16]. This corresponds to a brightness B of about 5×10^5 photons $\mathrm{m}^{-2}\,\mathrm{sr}^{-1}\,\mu\mathrm{s}^{-1}$. This value should be roughly doubled to account for long term atmospheric airglow. Moonlight at quarter phase doubles the amount of background light while at full phase it makes the night sky more than 10–20 times as bright, completely eliminating the possibility of detector operation during such times.

The sky brightness fluctuates during the course of a night but typically by no more than a factor of two from detector turn-on to turn-off. More troublesome are local wandering "hot spots" caused by certain stars, planets and the milky way disk. The average brightness seen by a Fly's Eye PMT corresponds to about a first magnitude star. Hence, when a star or planet brighter than this (about 15 or so in the northern hemisphere) enters a PMT field of view the dc background more than doubles (in the case of Venus, it climbs 10-fold!). This situation has been handled by programming all input thresholds to keep count rates constant.

3. Fly's Eye parameters

Establishment of design parameters for the Fly's Eye detector depends not only upon estimates of signal strength and noise but also upon the kinematics of the EAS signal source. The conversion of "apparent" brightness to "intrinsic" brightness depends upon accurate geometrical reconstruction of the observed track. In this section, we discuss the kinematics of an EAS as seen by the Fly's Eye detector and outline the technique employed to reconstruct the geometry of a shower. We then complete the appraisal of signal to noise and discuss the resultant implications for detector optimization.

3.1. Kinematics

An EAS trajectory appears as a sequential track propagating along a great circle projected upon the celestial sphere. The PMT "hit pattern" determines a plane in space within which the EAS trajectory lies. Shown in fig. 5 is the trajectory of an EAS as seen by the Fly's Eye. Four parameters are necessary to completely specify the EAS geometry. The shower-detector plane is specified by two parameters, the azimuthal and zenith angles of the unit vector $\boldsymbol{n}$ normal to the plane. This vector can easily be found by minimizing $\Sigma \boldsymbol{r}_i \cdot \boldsymbol{n}$ where $\boldsymbol{r}_i$ represents the ith observation direction vector toward a source on the EAS.

The timing sequence of the light pulse arrival times can be used to determine two additional parameters which characterize the orientation and distance of the EAS trajectory relative to the Fly's Eye. The expected timing sequence is derived from the fact that an EAS propagates in a straight line at the speed of light. Thus, the light reaching the observer from any point P (see fig. 6) is delayed from the arrival time of the passing shower front by a time

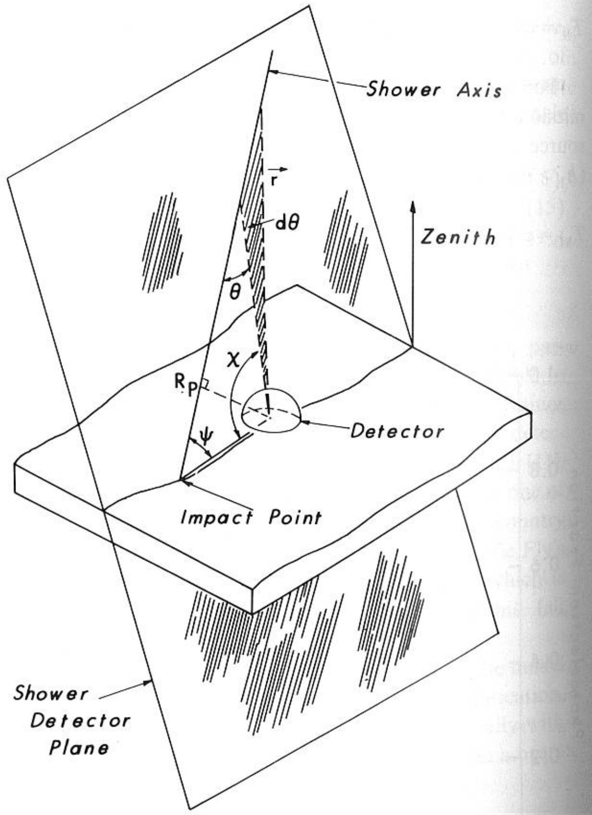

Fig. 5. Geometry of an EAS trajectory as seen by the Fly's Eye. The shower-detector plane contains both the EAS shower and the center of the Fly's Eye detector. It is specified by fits to the spatial pattern of "hit" PMTs which must lie along a great circle on the celestial sphere. The angle ψ and impact parameter R_p are obtained by fits to observation angles χ_i vs time of observation.

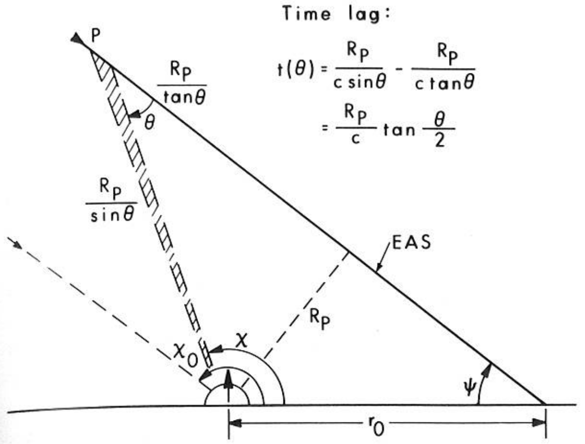

Fig. 6. Kinematics of EAS timing. Light received at the Fly's Eye from a point P on the EAS trajectory lags behind the light arriving from ∞ (or the time of passage of the EAS shower front) by a time: $\delta t(\theta) = R_\mathrm{p}/(c \sin\theta) - R_\mathrm{p}/(c \tan\theta) = (R_\mathrm{p}/c)\tan(\theta/2)$.

$$\delta_t(\theta) = \frac{R_\mathrm{p}}{c\sin\theta} - \frac{R_\mathrm{p}}{c\tan\theta} = \frac{R_\mathrm{p}\tan\theta/2}{c}, \tag{22}$$

where θ is the light emission angle from the shower axis. From fig. 6 it can be seen that

$$\chi_0 = \chi_i + \theta, \tag{23}$$

where χ_i is the observation angle in the shower-detector plane of the ith phototube and χ_0 represents the direction of the approaching shower. Thus

$$\chi_i(t_i) = \chi_0 - 2\tan^{-1}\big(c(t_i - t_0)/R_\mathrm{p}\big). \tag{24}$$

A best fit of the observed $\chi_i(t_i)$ to this function yields the parameters R_p and χ_0 which completes the specification of the EAS trajectory.

Application of the above reconstruction technique yields fairly accurate results for tracks whose lengths exceed a total subtended angle on the order of 50° or so. Between 30° and 50° the technique can be applied but with minimal accuracy obtained for the fitting angle χ_0. The accuracy obtained for the impact parameter R_p, even down to track lengths on the order of 30°, typically remains quite good, usually to better than ±30%.

If a shower is seen by both Fly's Eyes I and II, a best shower–detector plane for each detector can be determined and the intersection of those planes defines the shower trajectory. In addition, for each event observed by the two detectors in coincidence, a timing marker is sent via an infrared optical flash from Fly's Eye I to Fly's Eye II which permits clock synchronization to within ±100 ns. Thus, for each such event, including the degenerate coplanar case where direct stereoscopic reconstruction fails, a technique relying simultaneously upon the extended geometry of both detectors and absolute time recordings of all hit PMTs regardless of position (either at FEI or FEII) has been used to obtain the final geometry of the observed track.

3.2. Detector optimization

Using the constraints imposed by the kinematics and signal of an EAS event as well as the noise caused by the not-too benign night sky we can now estimate the parameters required of a reasonably optimal Fly's Eye detector if extensive air showers are to be seen via atmospheric fluorescence. Clearly, any given eye in the Fly's Eye detector must be endowed with sufficient light gathering power and angular resolution to pick out the signal generated by an EAS against random night sky noise. Secondly, since light from a shower is "compressed" in time during approach and "stretched out" in time when receding (see eq. (22)) and since 1 km $\lesssim R_\mathrm{p} \lesssim 20$ km, the electronics must have a wide dynamic range in time which greatly complicates trigger optimization.

For the purposes of making conservative estimates of required detector parameters, we will consider only the fluorescence signal which is $N_\gamma \approx 4$ photons/(electron m) (eq. (1)). From fig. 6 we see that in a time Δt, the EAS source as seen by the detector moves a distance

$$\Delta L = \Delta\left(R_\mathrm{p}/\tan\theta\right) = c\Delta t(1+\cos\theta)/\sin^2\theta, \tag{25}$$

and the number of photons reaching the detector is

$$\begin{aligned} N_\mathrm{ph} &\cong N_\mathrm{e} N_\gamma \Delta L\, A\, \mathrm{e}^{-r/\lambda_\mathrm{R}}/4\pi r^2 \\ &= N_\mathrm{e} N_\gamma \frac{(1+\cos\theta)}{\sin^2\theta} \frac{A}{4\pi r^2} \mathrm{e}^{-r/\lambda_\mathrm{R}} c\Delta t, \end{aligned} \tag{26}$$

where A is the optical gathering area of a Fly's Eye mirror and λ_R is the Rayleigh scattering length. Letting ε be the overall optical efficiency for converting photons into photoelectrons and noting that $R_\mathrm{p} = r\sin\theta$ we obtain the number of signal photoelectrons S generated in a time Δt during which the track is in view of that PMT

$$S = N_\mathrm{e} N_\gamma c \frac{(1+\cos\theta)}{4\pi R_\mathrm{p}^2} \mathrm{e}^{-r/\lambda_\mathrm{R}} A\varepsilon\Delta t. \tag{27}$$

The background noise N, due primarily to fluctuations in the dc PMT current arising as a result of exposure to the ambient night sky background is

$$N \simeq (4\varepsilon A B \Delta\Omega \Delta t)^{1/2}, \tag{28}$$

where B is the night sky starlight background and $\Delta\Omega$ is the solid angle seen by a single PMT. The factor of 4 is used to account for an effective increase in starlight background due to long term airglow and low energy cosmic rays as mentioned in the previous section. Hence the overall signal to noise σ is

$$\sigma = \frac{S}{N} \simeq N_e N_\gamma c \frac{(1+\cos\theta)}{4\pi R_p^2} e^{-r/\lambda_R} \left(\frac{\varepsilon A \Delta t}{4 B \Delta\Omega}\right)^{1/2}. \qquad (29)$$

Clearly, one optimizes signal to noise by maximizing ε, A, Δt and minimizing $\Delta\Omega$.

A few words about Δt are appropriate. Essentially, it is an integration time over which noise fluctuations are "smoothed out". A priori one does not know this time since it is event dependent. Events detected by the Fly's Eye can generate pulses whose widths range from 50 ns to 10 μs! Hence, to take full advantage of time integration in minimizing noise, we have employed a parallel triggering system with different time filters in order to trigger on nearby as well as distant events with optimum efficiency. Assuming optimized efficiency, Δt in eq. (29) can be approximated by $\Delta t \sim R_p \Delta\theta / c$. Furthermore, we note that $\Delta\theta$, the linear angular resolution of the detector and $\Delta\Omega$, the solid angle resolution, for an $f/1.0$ mirror can be expressed as

$$\Delta\theta = \frac{\mathrm{d}}{D} \quad \text{and} \quad \Delta\Omega \cong \frac{\pi d^2}{4 D^2}, \qquad (30)$$

where d and D are the diameters of the PMT and mirror aperture respectively. Neglecting the $\cos\theta$ angular factor, we obtain

$$\sigma = \frac{N_e N_\gamma}{8\pi} \left(\frac{c}{B}\right)^{1/2} \frac{e^{-r/\lambda_R}}{R_p^{3/2}} \left(\frac{\varepsilon D^3}{d}\right)^{1/2} \qquad (31)$$

for an estimate of signal to noise in terms of convenient detector parameters.

Final choice of detector parameters involves considerations other than signal to noise. In particular, enough points along the shower trajectory have to be sampled in order to accurately reconstruct the geometry of the shower as well as to provide reasonable resolution of the shower profile. Such considerations led us to the conclusions illustrated in fig. 7, in which are plotted the number of phototubes actually needed to image the entire sky along with time and cost of Fly's Eye construction in order to achieve a given angular resolution and number of track sampling points. From such an analysis, we concluded that 880 PMTs with an angular resolution of $\Delta\theta \sim 0.09$ radians and $\Delta\Omega \sim 0.066$ sr would be required for a reasonably optimal Fly's Eye detector.

Resultant energy triggering thresholds and event rates depend on the actual signal to noise value practically obtainable. We estimated during design studies that a 4σ triggering threshold should be achievable and would result in only a few noise triggers per event. Given that the noise spectrum is so steep, only mildly lower triggering thresholds would jam the system, while higher ones would result in loss of data. Actual noise rate measurements summed over 880 tubes looking at all directions in the clear night sky are shown in fig. 8. Also indicated is the threshold required to maintain a single PMT count rate at 50 Hz. The line superimposed on the data is the upper tail area function of a Gaussian probability distribution which describes the data almost exactly. The equivalent σ scale is shown along the upper x-axis. It can be seen that resultant thresholds correspond almost exactly to 4σ as expected. Since thresholds are automatically set by computer to fix PMT count rates at 50 Hz, the Fly's Eye detector is always as sensitive as it can be.

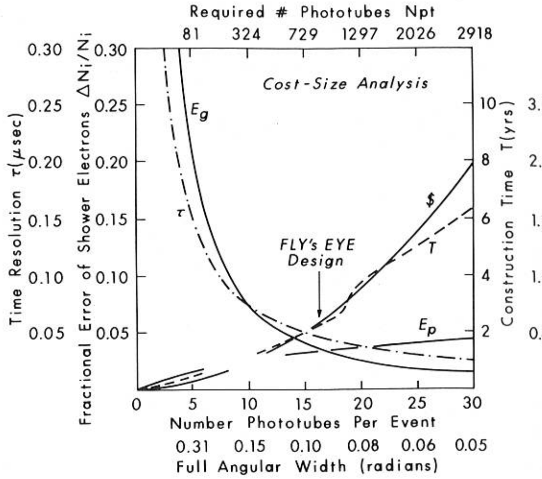

Fig. 7. Design–cost optimization. Five curves are shown: Error in shower size determination due to errors in (1) geometrical reconstruction ε_g or (2) photoelectron statistics ε_p vs number of viewing cells of given angular aperture along the bottom axis. The number of such cells required to completely image the entire sky is shown on the upper axis. The other curves include (3) the time resolution τ required for the electronics servicing each cell, (4) the time T and (5) the money \$ required to construct a Fly's Eye.

Finally, we convert electron size N_e to energy in order to obtain an estimate for energy triggering thresholds and event rates. We take [17]

$$E \simeq 1.6 \times 10^{-9} N_e \qquad (E \text{ in EeV}). \qquad (31)$$

Also, letting $D = 1.6$ m and $d = 5.5$ in., final values chosen for mirror diameter and PMT aperture to achieve the previously mentioned angular resolution factors, we obtain

$$E(\mathrm{EeV}) \cong 0.1\, R_p^{3/2}\, e^{R_p/\lambda_R} \qquad (R_p \text{ in km}), \qquad (32)$$

where all angular factors have been ignored. Thus, it should be feasible to trigger on EAS showers of energy $E \sim 0.1$ EeV at $R_p \sim 1$ km and $E \sim 100$ EeV at $R_p \sim 20$ km. Shown in fig. 9 is a scatter plot of E vs R_p for approximately 4000 real events detected by the Fly's Eye. The solid line (eq. (32)) represents the above simple estimate of minimum energy required for detectability at any R_p. Clearly, the simple analysis presented here is approximately correct. The events below the line at small impact parameters represent Cherenkov assisted triggers. Using the current best estimate for the integral cosmic ray spectrum [18] we obtain rough estimates for anticipated number of triggers per year

$$N(>E) = I(>E) A_\Omega^*(E) t, \qquad (33)$$

where A_Ω^*(E) is the aperture of the Fly's Eye as a function of energy and $\tau \sim 2 \times 10^6$ s, the amount of observing time available each year. We obtain

$$\begin{aligned} E > 0.1 \text{ EeV}: \quad & I = 3 \times 10^{-10} \text{ m}^{-2} \text{ sr}^{-1} \text{ s}^{-1}, \\ & A_\Omega^* = 10^7 \text{ m}^2 \text{ sr, N} \simeq 6000 \text{ events}, \\ E > 100 \text{ EeV}: \quad & I \simeq 4 \times 10^{-16} \text{ m}^{-2} \text{ sr}^{-1} \text{ s}^{-1}, \\ & A_\Omega^* \simeq 10^9 \text{ m}^2 \text{ sr}, N \simeq 1 \text{ event/y} \end{aligned}$$

as event rates that can be anticipated for a Fly's Eye detector with parameters outlined in table 1.

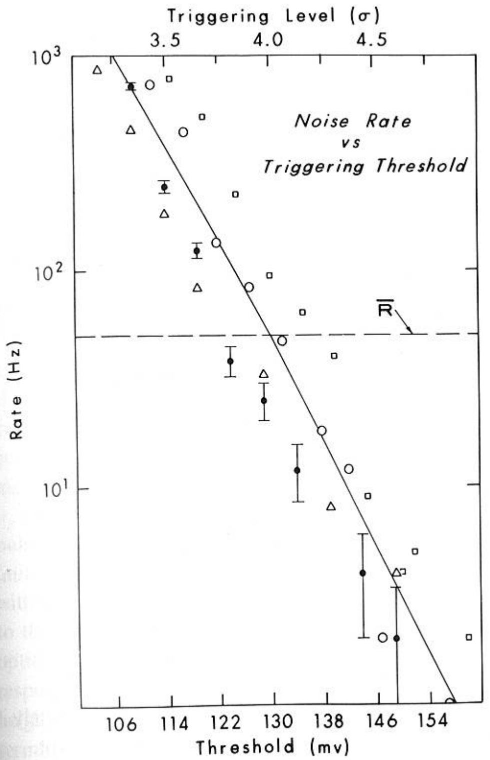

Fig. 8. Noise rates vs threshold and equivalent signal to noise ratios $\sigma = S/N$. The curve through the data represents the upper tail area function of a Gaussian distribution. The data points represent sums over 880 tubes looking in the five zenith angle rings comprising the Fly's Eye, ranging from $\theta_z = 0°$ out to $\theta_z \sim 82.5°$. Fixing PMT counting rates at 50 H_z effectively forces triggering at a signal to noise ratio of 4.0.

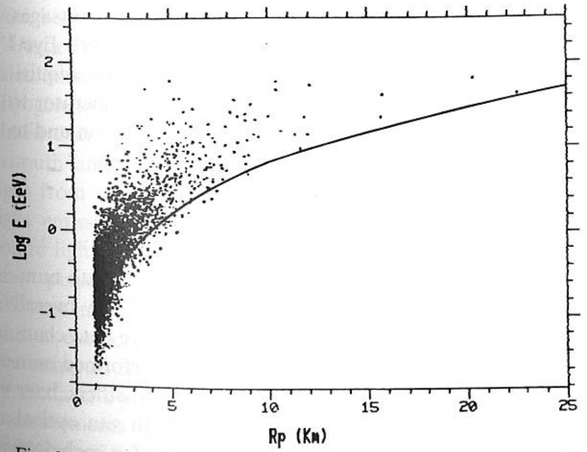

Fig. 9. Distribution of shower energy E vs impact parameter R_p for approximately 4000 events. The line represents a simple estimate of the minimum detectable energy given by: E(EeV) $= 0.1\ R_p^{1.5} e^{R_p/\lambda}$, where λ is the Rayleigh scattering length ~ 18 km.

Table 1
Fly's Eye detector parameters

Number of mirrors	FE I: 67, FE II: 8
Diameter of mirror	1.575 m
Focal length	1.50 m
Number of PMT (and Winston cones)	FE I: 880, FE II: 112
Mirror obscuration	13%
Mirror–cone efficienct product	~ 70%
PMT	EMI 9861B
Peak quantum ε at 360 nm	0.21
Angular aperture/PMT	91.5 mr
Solid angle/PMT	6.57 msr
Number of electronics channels	FE I: 2640, FE II: 336
Charge dynamic range	10^5 linear
Time resolution	25 ns

4. Detector operation

4.1. Electronics and software

The Fly's Eye detector operates under computer control. Main control functions deal with automatic adjustment of thresholds to maintain constant count rates at the 4σ triggering level. Simply raising thresholds and running "open loop" is obviously possible but would result both in reduced aperture as well as a loss of track length information which would severely compromise geometrical reconstruction. Control also exists for changing trigger requirements, activating and deactivating specific sensors, monitoring light collection efficiency, both external and internal temperatures, electronic gains and pedestals, positioning mirrors and exposing photomultipliers to the night sky.

Data acquisition software runs on a PDP 11/34 with 128 Kwords of memory, a 30 Mbyte Winchester disk,

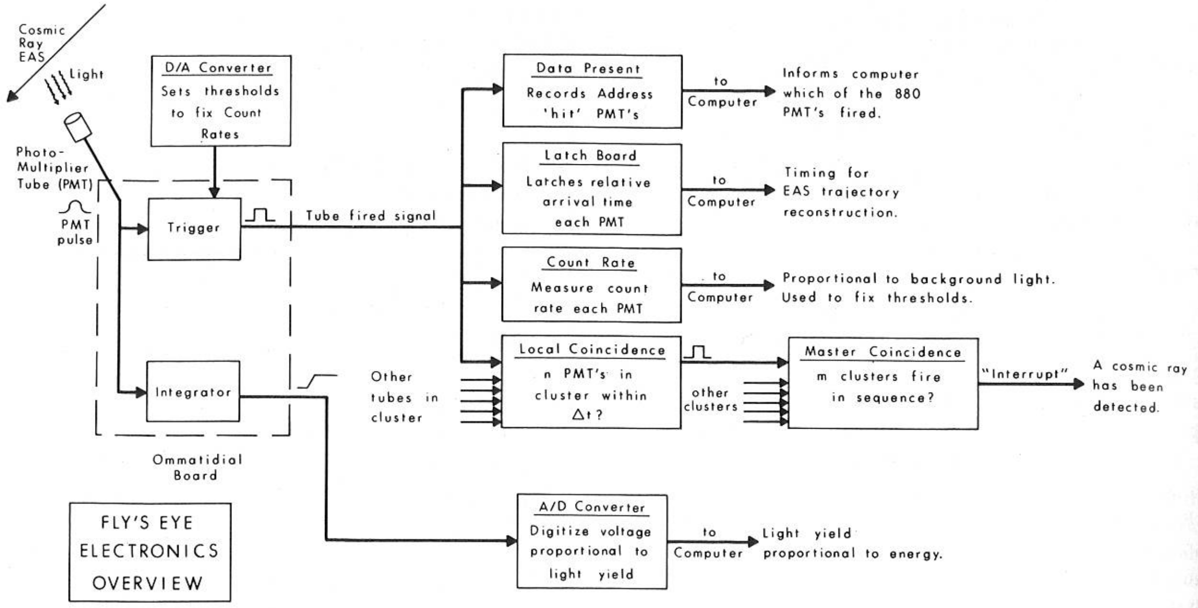

Fig. 10. Block diagram of the Fly's Eye data acquisition electronics.

and 3 RK05 2.5 Mbyte disks. The operating system currently in use is Digital Equipment Corporation's RSX-11M v4.0, a real-time, multi-tasking software system. Data acquisition is interrupt-driven with all I/O performed under programmed, parallel I/O via a number of 16 bit I/O external data busses connected to the PDP 11/34 unibus via DEC's DR11 parallel interface units.

When Fly's Eye triggering conditions are met, an interrupt is generated by the master coincidence unit which causes the computer to: (1) Read in all "hit" bits to determine which signal processing boards are holding analog information needing to be digitized and which timing "latch" boards are holding arrival time data. (2) Send commands to digitize and read in all pulse-integrals currently being held. (3) Digitize and read the operating thresholds of all PMTs that fired. (4) Read the latch timing boards to obtain the relative firing time of each PMT. (5) Read the precise time of day (±1 ms) from a WWVB clock. (6) Store all information on a disk file. (7) Pass relevant information to an LSI-11 computer which then displays the event in "real-time" on a 3 ft diameter hemispherical dome representing the celestial sphere. A block diagram of the data acquisition electronics which performs these tasks is depicted in fig. 10.

Typically, it takes about 1–10 ms to process a single event. Trigger rates are about 1 s^{-1} and dead time about 1%. All analog integrals can be held for 20 ms to within a few percent of their original value prior to digitization. Threshold adjusting to stabilize count rates at 50 Hz and any other currently executing tasks such as temperature and voltage monitoring are immediately suspended upon the occurrence of an event interrupt.

The main data acquisition task, among other things, monitors the operator's teletype keyboard for operator commands and performs them when called for. Commands include manual threshold control, activating and deactivating selected tubes, mirrors or groups of mirrors, changing running parameters such as minimum and maximum thresholds, count rate intervals and windows, trigger requirements, plotting histograms, recording all temperatures from a large array of both external and internal temperature sensors, getting status reports, displaying events, logging operator messages, monitoring the infrared optical trigger from Fly's Eye I to Fly's Eye II, and enabling and disabling data acquisition. In general, these commands permit an operator to easily bring the Fly's Eye detector into operation and to quickly ascertain that it is performing properly.

4.2. Optical calibration

Converting measured photoelectron yields into numbers of photons requires a knowledge of the overall efficiency-gain product εG_i of each Fly's Eye data channel. An absolute measurement has been performed on a single channel and the εG factors of all others have been obtained by relative normalization. In situ optical pulsers continually monitor the εG factors for each data channel at all times subsequent to the time of absolute calibration.

Absolute PMT quantum efficiencies, mirror and Winston cone reflectivities were measured in the laboratory and the following values obtained $\varepsilon_{\text{pmt}} = 0.212 \pm 0.015$, $\varepsilon_{\text{cone}} = 0.80 \pm 0.05$ and $\varepsilon_{\text{mirror}} = 0.83 \pm 0.04$ giving an overall product efficiency of $\varepsilon = 0.141 \pm 0.016$. The gain factor G includes PMT gains, preamplifier transconductance, finite cable dc resistance, charge-integrator board input impedance and voltage-time input to digitized voltage output conversion factors. The resultant overall gain is:

$$G = 0.757 \pm 0.076 \text{ mV/photoelectron}.$$

Thus, the absolute number of quanta seen by the ith PMT is $N_{\gamma i} = V_i/(\varepsilon G \eta_i)$, where V_i is the digitized voltage and η_i is the ratio of teh εG factor of the ith data channel to that of the one whose absolute value is known. Typically, values of η_i are known to ±5% accuracy. Hence, errors in absolute quanta measurements, δN_γ, are on the order of ±16%.

Relative efficiencies η_i are monitored by optical pulsers permanently installed in each mirror housing unit. The optical pulser consists of an argon flash bulb with an optical fiber bundle to transmit the light flash to the mirror's focal plane. On computer command, an optical flash illuminates each mirror uniformly and the response from every PMT is recorded. Resultant pulse height distributions (~ 1.5% fwhm) are used to determine all relative efficiencies η_i on a nightly basis. Each year, a new absolute measurement on the standard channel is performed and all in situ optical pulsers are re-calibrated. None have been found to drift more than 3% between absolute calibrations.

Overall absolute efficiencies for all 1000 tubes typically degrade no more than 20%/y. Efficiency loss is due primarily to tube gain drift and mirror-cone reflectivity degradation. All mirrors are cleaned and re-aluminized once a year to recapture efficiencies. Winston cones are protected from the environment somewhat better and need replacement once every 2–3 y.

As a final check on optical calibration (as well as calculations of Rayleigh and Mie scattering) a pulsed nitrogen laser has been installed at Fly's Eye II and aimed over Fly's Eye I at a variety of different zenith, azimuth angles and impact parameters. The scattered light from the upward-going laser light pulse simulates light emission from an extensive air shower. The absolute light yields measured by the Fly's Eye for each laser pulse can be used to calculate the number of photons in the pulse given a knowledge of its trajectory and a correct treatment of both Rayleigh and Mie scattering as outlined in sect. 2. The resultant estimates of the laser's photon source strength based on Fly's Eye measurements of the scattered light agree with direct measurements of the laser output to within 20%. The agreement obtained implies that (1) absolute Fly's Eye optical calibration is well known to within estimated experimental errors, and (2) the treatment of Rayleigh and Mie scattering of a propagating light beam through the atmosphere has been treated adequately.

4.3. Checks on geometrical reconstruction

The techniques of track reconstruction described in sect. 3 have been applied to a series of "upward-going" showers generated by an array of collimated xenon flashers which are permanently positioned around the Fly's Eye detector. The flasher units are battery powered and activated by photodiode sensors to fire at two hour intervals between sunset and sunrise. A permanent flasher has also been installed at Fly's Eye II and aimed over Fly's Eye I. This unit is triggered to within ±1 ms by a WWV clock every hour on the hour, thus providing an accurate time fiducial for each Fly's Eye well as a spatial fiducial for Fly's Eye I. In addition, a mobile xenon flash unit was fired vertically from each of 20 equally-spaced azimuthal positions on a 2 km radius circle around Fly's Eye I. Thus, fiducial tracks have been generated for every mirror in the Fly's Eye detector. As a final check the nitrogen laser was fired over Fly's Eye I at a variety of angles and impact parameters to search for any systematic geometry-dependent reconstruction problems.

Shown in figs. 11 and 12 is an example of the reconstruction of a trajectory generated by measuring the scattered light of a laser pulse. Fig. 11 illustrates the fitting technique employed to determine the shower-detector plane. The figure is a projection of the celestial sphere onto a horizontal plane. Zenith (due overhead) is located in the geometric center while the horizon is represented by the dashed circular line. Each "hit" PMT is given by a number with each number representing the firing time order. X's represents noise, i.e., hits which occurred during the event gate but correlated neither in time nor space with the real event PMT's. The line through the track represents the best plane fit.

Fig. 12 illustrates a fit of the function given by eq. (24) to the observing angles vs arrival time. Resultant geometrical parameters obtained for the event are shown in the insert. The laser was actually fired at a zenith angle of 65° and impact parameter of 1.31 km, in excellent agreement with track parameters obtained from the fit.

Shown in figs. 13a and 13b are distributions of the difference in zenith angle $\delta\theta_z$ and impact parameter δR_{p} from known values for all vertical-going xenon flasher pulses generated at the 20 equally-spaced azimuthal positions around Fly's Eye I. The rms reconstruction errors for all these trajectories are 1.7° and 100 m respectively. The non-Gaussian tails in the distributions are due to the presence in the data of a wide variety of track lengths ranging from 40° to 120° each of which is Gaussianly distributed with a different width. The most probable fitting error estimated for all events is 1.7° which agrees with the σ of the distribution of fig. 13a. We infer that inaccuracies inherent in the geometrical reconstruction process are well-understood.

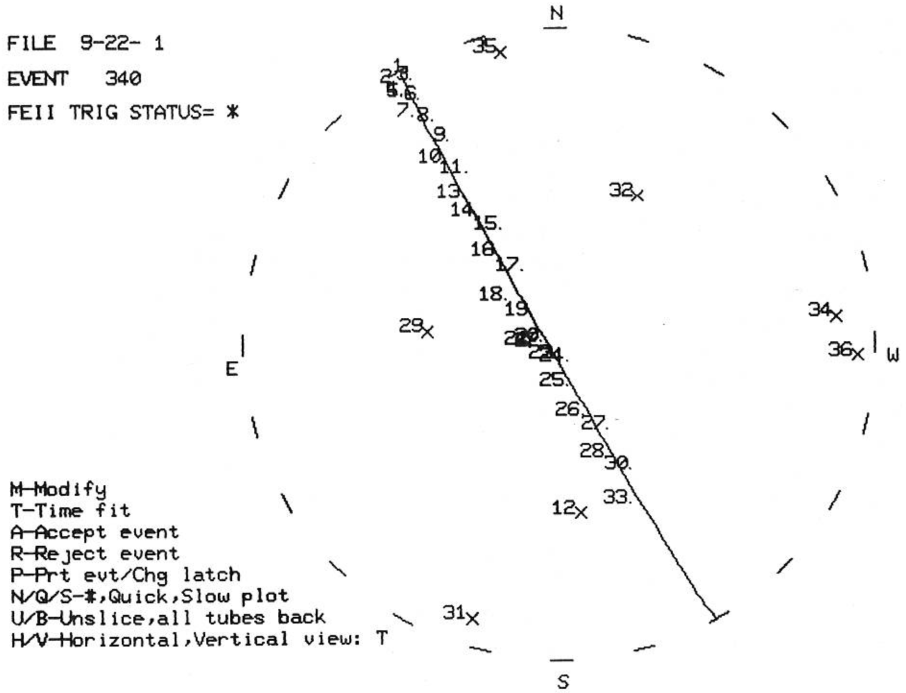

```
FILE  9-22- 1
EVENT   340
FEII TRIG STATUS= *

M-Modify
T-Time fit
A-Accept event
R-Reject event
P-Prt evt/Chg latch
N/Q/S-#,Quick,Slow plot
U/B-Unslice,all tubes back
H/V-Horizontal,Vertical view: T
```

Fig. 11. Reconstruction to a track generated by a 10^{13} photon N_2 laser pulse propagating up over the Fly's Eye and out of the atmosphere. The numbers represent PMT firing time order. The X's represent noise pulses correlated neither in space or time with the real event. The dashed-line is the horizon; straight overhead is in the geometric center and the line represents a best fit for the "shower-detector" plane.

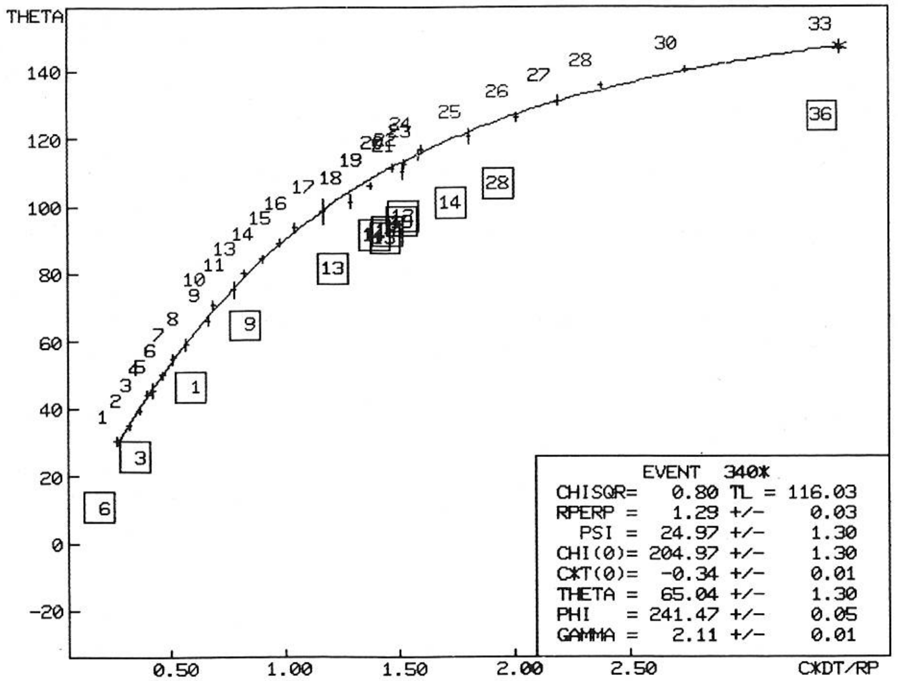

```
        EVENT  340*
CHISQR=   0.80 TL = 116.03
RPERP =   1.29 +/-    0.03
  PSI =  24.97 +/-    1.30
CHI(0)= 204.97 +/-    1.30
C*T(0)=  -0.34 +/-    0.01
THETA =  65.04 +/-    1.30
PHI   = 241.47 +/-    0.05
GAMMA =   2.11 +/-    0.01
```

Fig. 12. Timing plot for the laser event of fig. 10. Theta is the angle in degrees between the laser pulse trajectory and the line of sight to the Fly's Eye. The boxes contain the mirror number while the individual numbers represent the particular PMT which saw the light pulse. The x-axis represents the arrival time difference $c\delta t/R_p$ normalized to the fitted impact parameter R_p. Event parameters are contained in the figure's insert. The laser was actually fired at $R_p = 1.31$ km, zenith angle $\theta_z = 65°$, and $\psi = 25°$.

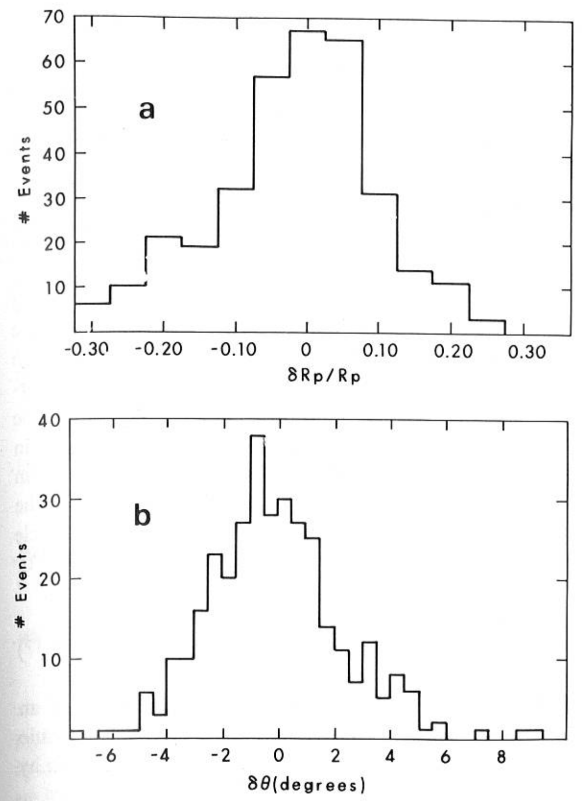

Fig. 13. Distributions of reconstructed (a) zenith angle and (b) impact parameter deviations from known values for 20 fiducial xenon flashers located at 18° azimuthal intervals around the Fly's Eye detector. Fiducial tracks from these flashers have been generated through the field of view of every mirror in the Fly's Eye array. The σ's of the distributions are 1.7° in zenith angle and 100 m (out of 2 km) in impact parameter.

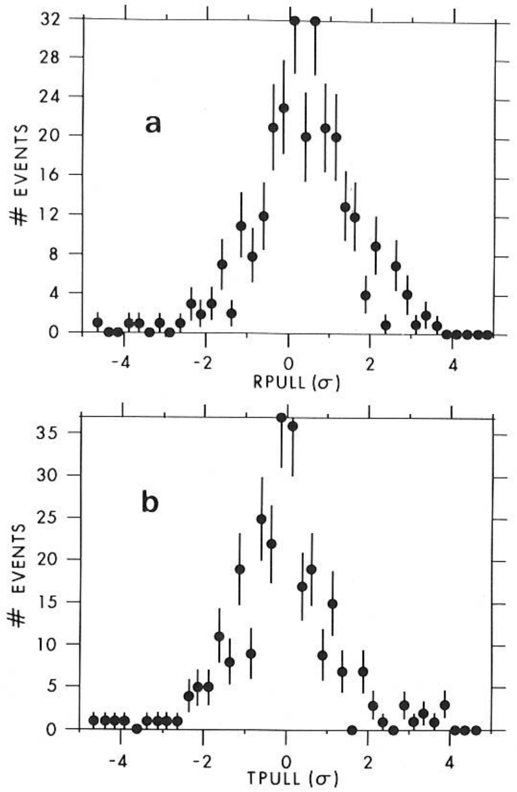

Fig. 14. Distribution of measured (a) impact parameter deviations RPULL $= \delta R_p/(\sigma_1^2 + \sigma_2^2)^{1/2}$ and (b) zenith angle deviations TPULL $= \delta\theta_z/(\sigma_1 + \sigma_2^2)^{1/2}$ between single eye (1) reconstructions and double eye (2) reconstructions. The distributions should be Gaussian with a 1σ width if errors are properly estimated. A small (about 1/3σ) systematic shift can be seen in the R_p data which implies that single eye reconstructed events may have slightly larger impact parameters than estimated.

Finally, in figs. 14a and 14b, we show the distribution of differences in θ_z and R_p obtained by single eye and steroscopic reconstruction for a sample of real events observed simultaneously by Fly's Eye I and II. Each difference has been normalized to the rms value of the sum of squares of the single eye and stereo fitting errors on an event by event basis, thus "pulling" the resultant distribution towards a Gaussian of anticipated width 1σ. Indeed, the resultant distributions are essentially Gaussian and no systematic differences within anticipated errors are to be found.

5. Data analysis

5.1. Size and total energy measurements

The chief virtue of the Fly's Eye detector is its advertized ability to make total energy measurements calorimetrically in a model-independent way. The analysis procedure is carried out in several stages. First, trajectory parameters are reconstructed as previously described. An example of applying both single eye as well as steroscopic reconstruction to an event observed simultaneously by Fly's Eye I and II is shown in figs. 15 and 16. Resultant geometrical parameters and associated errors are indicated in the figure inserts. Also, during this stage of analysis, pulse integrals for each PMT are corrected for pedestals and relative efficiencies and then converted into photoelectron yields.

During the next stage of analysis, the EAS longitudinal size N_e as a function of atmospheric slant depth is calculated using an iterative process to remove the photoelectron contributions due to the direct and scattered Cherenkov beam. Shower size at the calculated depths is then determined from the number of residual photoelectrons presumably due to the atmospheric scintillation process. Finally, each resultant longitudinal profile is fitted with two functions in order to obtain best estimates of (1) the shower size at maximum development

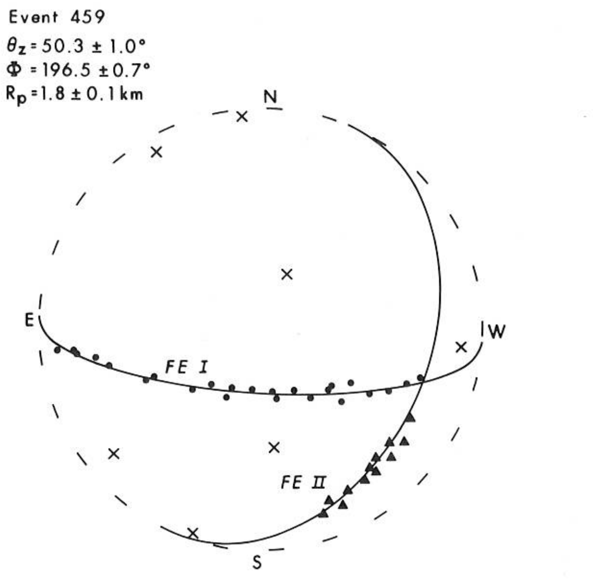

Fig. 15. Stereoscopic reconstruction of an event seen simultaneously by Fly's Eye I and II. The lines drawn thru the dots (indicating "hit" PMTs at each eye) represent the best fit for each of the two shower–detector planes. The intersection of the two planes gives the EAS trajectory whose parameters are indicated above the figure.

$N_{\max}$, (2) the location of maximum development $X_{\max}$, and (3) the track length integral of the longitudinal development profile $\int N_e(x)\mathrm{d}x$. The two functions used are: (1) An unconstrained (3 free parameters) Gaisser–Hillas shower development function of the form [17]

$$N(x) = N_{\max}\left(\frac{x - x_o}{X_{\max} - x_0}\right)^{(X_{\max} - x_0)/\lambda} \mathrm{e}^{(X_{\max} - x)/\lambda}, \quad (36)$$

where x_0 is the depth of first interaction and $\lambda = 70$ g cm^{-2} and (2) a Gaussian. An example of applying these two fits to the size data is shown in fig. 17. Even though the Gaisser–Hillas and Gaussian functions have different shapes the integral of the shower $\int N_e \mathrm{d}x$ can be estimated directly from either of these two fits with an accuracy indistinguishable from each other or from estimates based upon direct numerical integration of the data points. Finally, the energy of the primary particle is obtained from the integral of either the Gaussian or Gaisser–Hillas integral:

$$E = \frac{\varepsilon_0}{x_0}\int N_e(x)\mathrm{d}x, \quad (37)$$

where ε_0/x_0 is the ratio of the critical energy of an electron to the radiation length in air [18]. This ratio converts track length integrals into total energy loss by

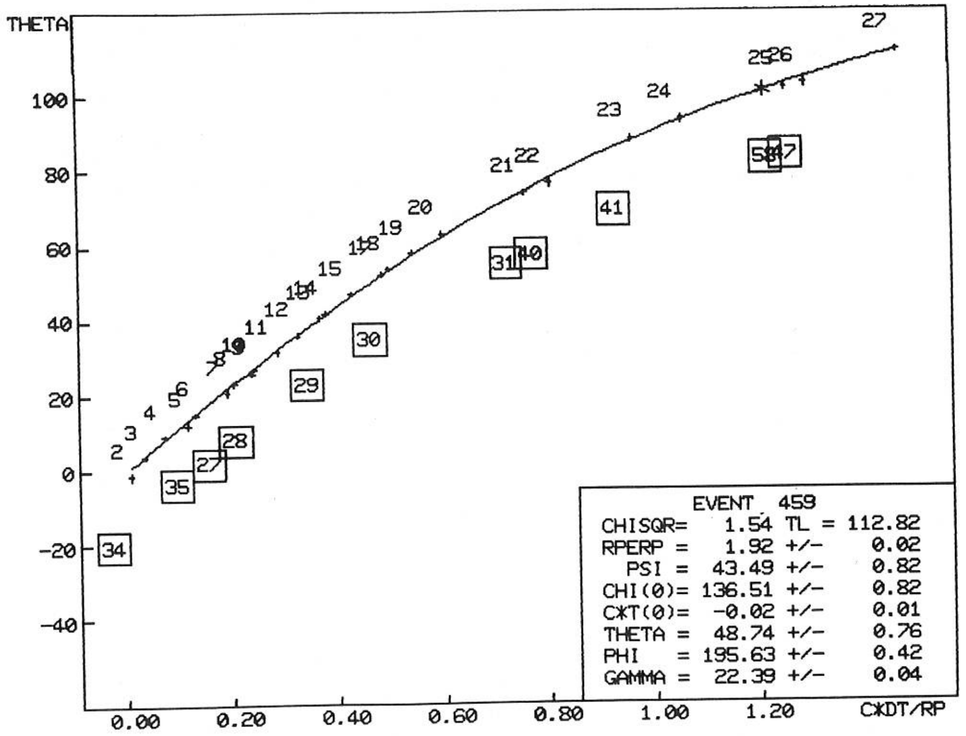

Fig. 16. Timing fit for Fly's Eye I data only for the same event reconstructed stereoscopically in fig. 15. The geometrical parameters (R_p, θ_z, ϕ, etc.) reconstructed by each technique agree within errors.

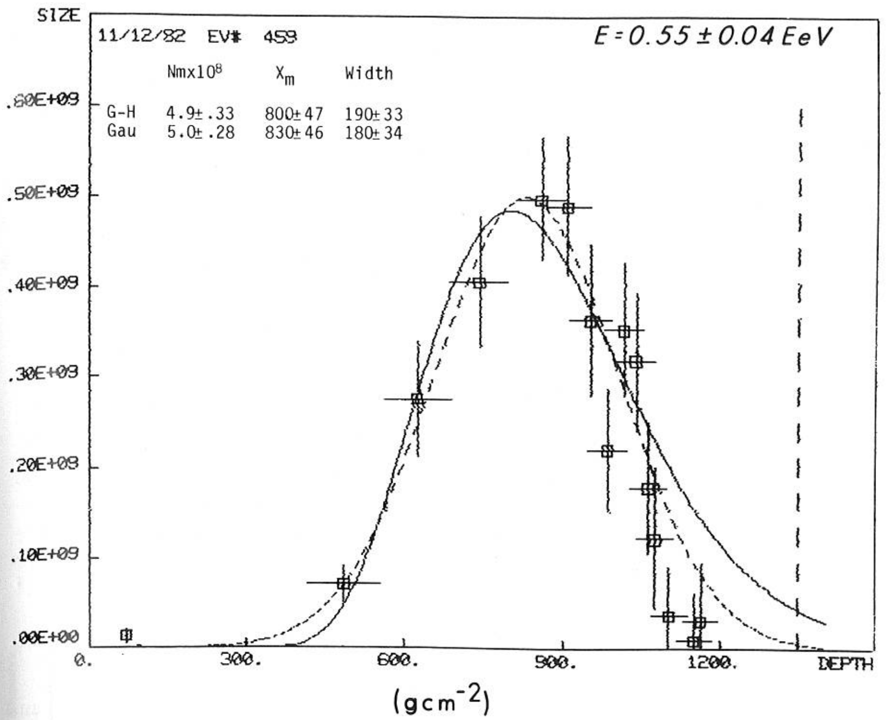

Fig. 17. Shower development curve (numbers of electrons vs atmospheric slant depth). Two fits have been employed to estimate shower parameters. (1) a Gaisser–Hillas (solid line) and a (2) Gaussian (short dashed line) fit. The parameters and associated errors are listed for each fit.

excitation and ionization [19]. We take $\varepsilon_0 = 81$ MeV and $x_0 = 37.1$ g cm^{-2} giving an energy loss rate of 2.18 MeV electron^{-1} g cm^{-2}. In additon, we apply roughly a 10% correction to account for undetected energy lost via: (1) undetected neutrals that fail to quickly decay into detectable charged particles before striking the ground, (2) a significant number of high energy muons or (3) nuclear excitation by the hadrons in the shower. We wish to point out that this particular assignment of energy to the incoming primary cosmic ray is *virtually independent of any high energy physics models, a situation that holds true for no other EAS detector of which we are aware*. The energy assigned to the shower depicted in figs. 15–17 is $E = (0.55 \pm 0.04)$ EeV while the size at maximum is $N_{\max}(5.0 \pm 0.28) \times 10^8$ electrons. The ratio $E/N_{\max} = 1.1$ GeV/electron is close to a value based upon Monte Carlo simulations of EAS in this energy region using high energy cross sections measured at accelerator energies along with radial scaling [20,21]. This value is also close to that estimated by Linsley [22] from a wide variety of cosmic ray data and in direct conflict with predictions based on Feynman scaling [23,24].

5.2. *Real vs Monte Carlo response*

A Monte Carlo simulation of the Fly's Eye detector has been performed in order to calculate the complicated energy-dependent detector aperture as well as to check the validity of the overall analysis procedure. An isotropic cosmic ray flux incident upon a model atmosphere [25] has been generated by selection from quasi-random trajectories and depths of first interactions. The resultant EAS is then developed according to a constrained (1 free parameter) Gaisser–Hillas shower development function with

$$(X_{\max} - X_0)/\lambda = 0.51 \ln(E/Ec) - 1$$

and $N_{\max} = E/1.64$ GeV, where $\lambda = 70$ g cm^{-2}. The light production mechanisms as outlined in sect. 2 are then invoked to calculate numbers of photons striking each PMT. The entire Fly's Eye optical system and signal processing electronics is modelled and those PMTs which generate pulse voltages above the 4σ triggering threshold are registered as "hits". Pulse integrals and arrival times are then stored for the "hit" PMTs. Timing jitter in the electronics is simulated by Gaussian fluctuations of the analytically calculated arrival times. The resultant simulated "data" are written onto a data file which can then be subjected to the same analysis procedure as that of the real data.

The self-consistency of the entire analysis procedure can be checked by examining resultant response functions (analyzed output parameters vs known Monte-Carlo inputs). Shown in figs. 18a–18c are response functions for shower zenith angle θ_z, impact parameter

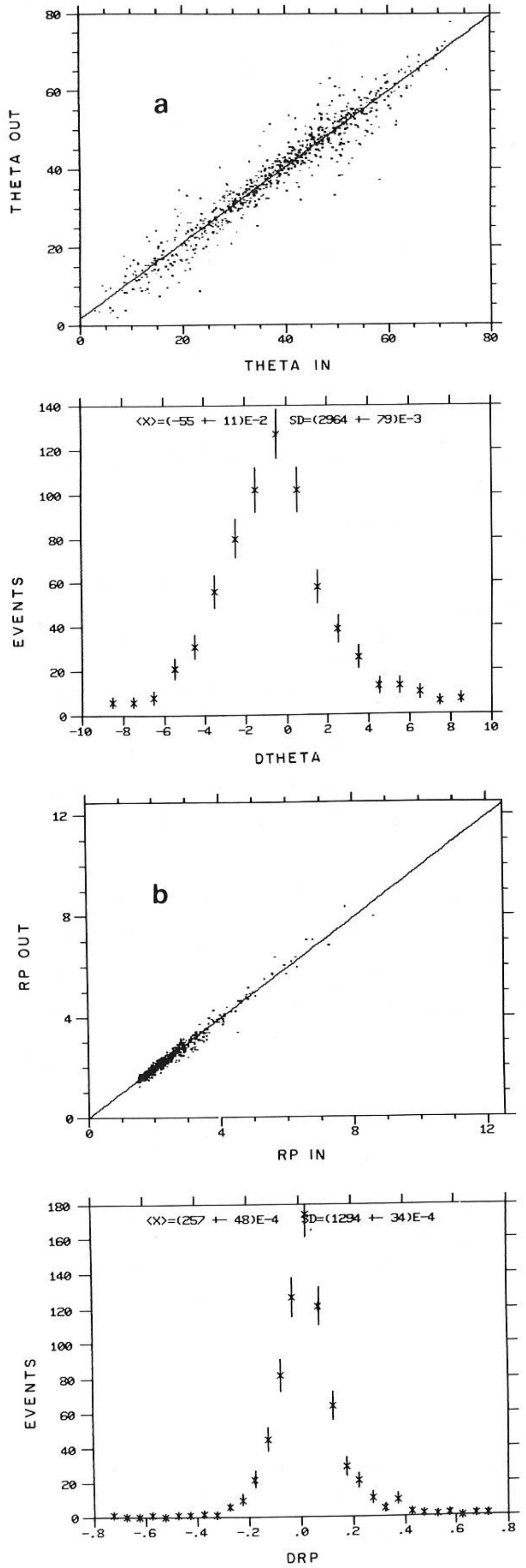

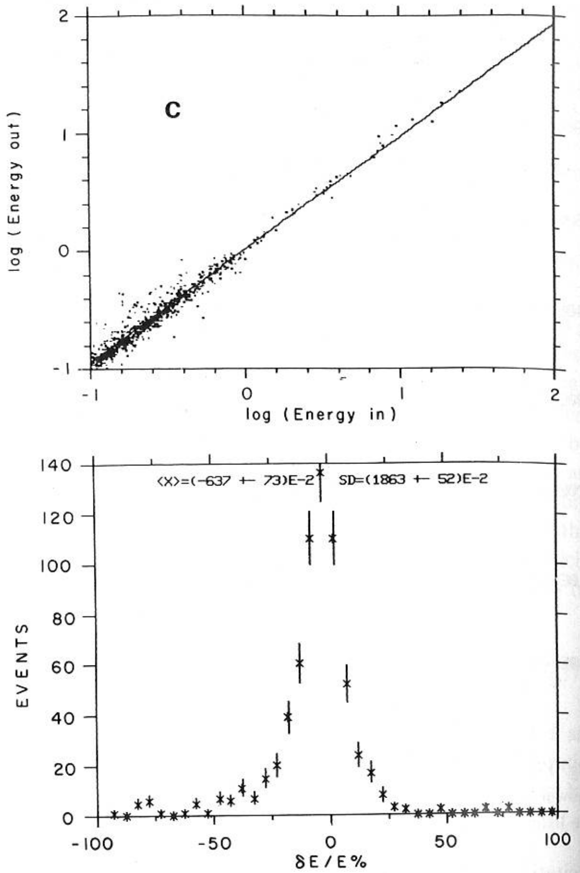

Fig. 18. Monte Carlo response functions. Analyzed output parameters obtained by Fly's Eye I reconstruction vs known Monte Carlo input parameters for (a) zenith angle θ_z, (b) impact parameter R_p and (c) shower energy E. Lower figures show the distribution of differences between output and input parameters.

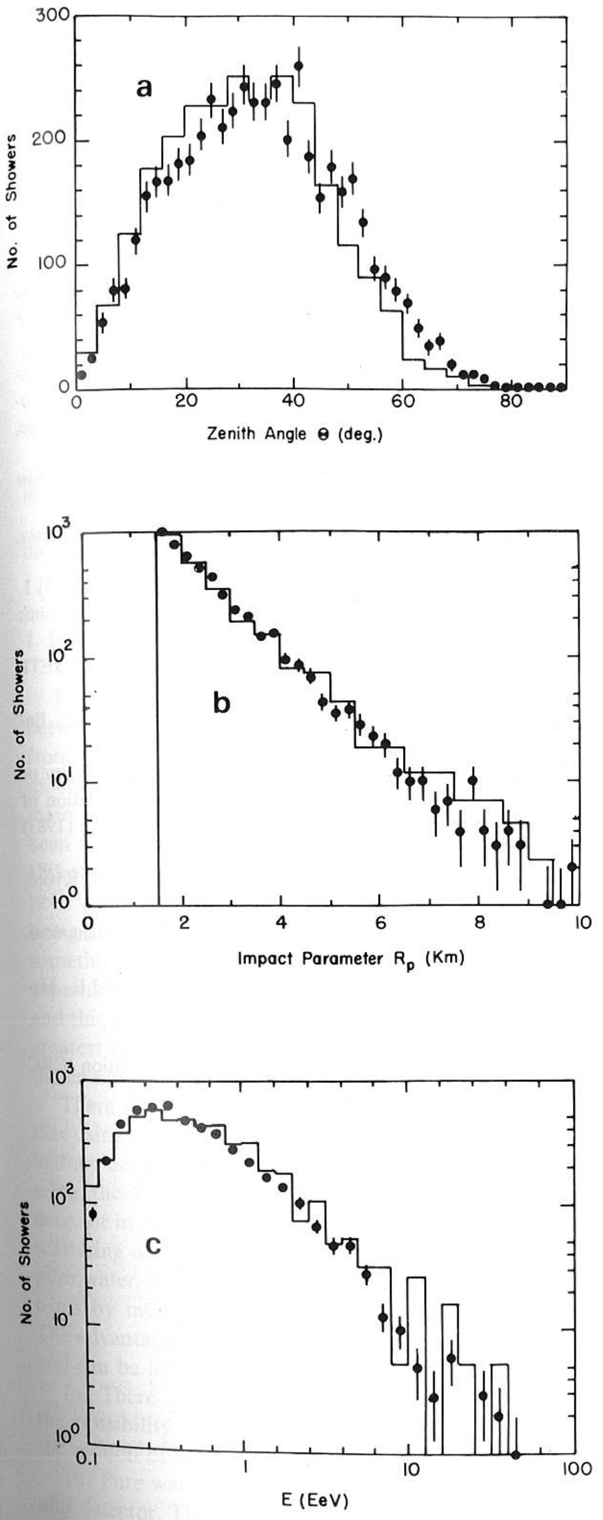

Fig. 19. distributions of shower parameters (a) θ_z (b) R_p (c) E. Real data are shown as a histogram without error bars. Monte Carlo data are shown as points with errors bars. All data have been selected such that the measured track length exceeds 50°.

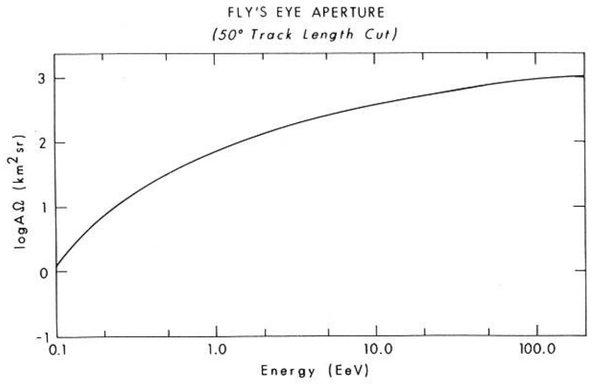

Fig. 20. Monte Carlo-calculated Fly's Eye I aperture A_Ω in km² sr for a 50° track length cut.

R_p, and energy E. Means and standard deviations are also indicated in these respective figures. It is clear from these figures that no systematic errors in the estimation of the primary particle parameters result from the analysis procedure.

In principle, the Monte Carlo can be used to obtain the most accurate estimates of primary cosmic ray spectra, anisotropies, composition and shower development profiles including the effects of fluctuations. In practice, adjusting a multitude of parameters until the best global agreement is obtained between real and Monte Carlo generated distributions, is likely to prove quite a tedious and time-consuming, if not impossible, endeavor. The Monte Carlo simulations have proven to be most sensitive to energy spectra. Consequently, efforts thus far have been directed towards obtaining an estimate of the energy dependent Fly's Eye aperture by selecting only "average" shower development profiles according to the Gaisser–Hillas parameterization allowing only for fluctuations in the depths of first interactions. The aperture is calculated by summing up the area-solid angle bins in which an event of energy between E and $E+\Delta E$ will produce a trigger. The differential rate of such events is

$$\frac{\mathrm{d}N}{\mathrm{d}E}=\int_{A_\Omega(E)} j(E)\,\mathrm{d}(A_\Omega(E)), \tag{38}$$

where $j(E)$ is the differential primary cosmic ray spectrum and $A_\Omega(E)$ is the acceptance in km² sr for events between E and $E+\Delta E$. Assuming that $I(E) \propto E^{-\beta}$, both the aperture and spectrum can be calculated by picking events of energy E weighted by $E^{-\beta}$ and adjusting β until best agreement is obtained between the real and Monte Carlo generated distributions. Plotted in figs. 19a–19c are the Monte Carlo data generated by picking events from a $1/E^3$ spectrum along with the real data distributions for the same parameters. Shown in fig. 20 is the resultant Fly's Eye triggering acceptance $A_\Omega(E)$. All of these distributions, both real as well as Monte Carlo, have been generated by demanding that the detected event subtend an angular track length of at least 50° in extent. It can be seen that good agreement is obtained in the energy region $0.5 < E < 10$ EeV. At lower energies, the finite spatial extent of showers (which can be detected only at distances close to the Fly's Eye) disperses the light source and degrades signal to noise from that calculated by the Monte Carlo. Furthermore, the rapidly-rising aperture in that energy regime is quite dependent on precise triggering details which have not yet been accurately modelled. Thus, the overestimate of event rates at lower energies is not disturbing and should not be construed as a spectral feature. At higher energies ($E > 10$ EeV) the electronic response of the detector is well-understood and triggering uncertainties should introduce no inaccuracies in aperture calculations which thus depend almost solely on the exact details of the applied data cuts and their effect on geometry.

6. Conclusion

Based on the detailed understanding of Fly's Eye performance obtained so far, we conclude that the detector should, with continued diligence, be able to achieve most of its designed goals. In particular, the goal of an accurate assessment of the high energy cosmic ray spectrum at energies exceeding the Greisen cutoff [26] at $E \simeq 60$ EeV appears to be well within reach, albeit at the current slow data rate of 20–30 events/y at $E > 10$ EeV. However, current modifications now underway call for the expansion of Fly's Eye II to 36 mirror units (instead of 8), installation of bialkali PMTs and UG-1 filters (which have been tested and found to enhance signal to noise ratios by a factor of 2) and reduction of the bandwidth of the fast triggering channel which, interestingly enough, lowers triggering thresholds for the slower, more remote and energetic events. We note that the most remote and energetic event seen so far was $E = 68$ EeV at $R_p = 22$ km. The above modifications should expand the viewing aperture to about 40 km and increase data rates at the high energy end of the spectrum by about a factor of 3–4. In addition, the increased aperture for events simultaneously seen by Fly's Eye I and II should result in the detection of 500–1000 events/y in the energy region 0.1–10.0 EeV with a resolution on the order of 50 g cm^{-2} making possible an accurate assessment of the primary cosmic ray composition.

We gratefully acknowledge the National Science Foundation for its support of this experiment.

References

[1] G.D. Rochester and K.E. Turver, Contemp. Phys. 22 (1981) 425.

[2] R.T. Hammond et al., Nuovo Cim. 1C (1978) 315.

[3] A.N. Bunner, PhD Thesis, Cornell University, Ithaca, NY (1964).

[4] R.W. Nicholls, E.M. Reeves and D.A. Bromley, Proc. Phys. Soc. 74 (1959) 87.

[5] R.H. Hughes, J.L. Philpot and C.Y. Fan, Phys. Rev. 123 (1961) 2084.

[6] F.I. Boley, Rev. Mod. Phys. 36 (1964) 792.

[7] K. Greisen, Ann. Rev. Nucl. Sci. 10 (1960) 63.

[8] W. Galbraith and J.V. Jelley, Nature, London 171 (1953) 349.

[9] A.M. Hillas, J. Phys. G 8 (1982) 1461.

[10] J.W. Elbert, T. Stanev and S. Torii, Proc, 18th Int. Conf. Cosmic Rays, Bangalore, India, 6 (1983) 227.

[11] E.C. Flowers, R.A. McCormick and K.R. Kurfis, J. Appl. Metereology 8 (1969) 955.

[12] L. Elterman and R.B. Toolin, Handbook of Geophysics and Space Environments, Ch. 7, Air Force Cambridge Research Labs, Office of Aerospace Research, USAF (1965).

[13] N.A. Baum, Stars and Stellar Systems, Astronomical Techniques, The Detection and Measurement of Faint Astronomical Sources vol. 2 (University of Chicago Press, Chicago, London) (1962) p. 1.

[14] J.W. Chamberlain, Physics of the Aurora and Air Glow (Academic Press, New York, 1961).

[15] C.W. Allen, Astrophysical Quantities (Athlone Presss, University of London, 1976).

[16] F.E. Roach, Advan. Electron. Electron Phys. 18 (1963) 1.

[17] T.K. Gaisser and A.M. Hillas, Proc. 15th Int. Conf. Cosmic Rays, Plovdiv, Bulgaria 8 (1977) 353.

[18] O.I. Dozkhenko and A.A. Pomanskii, Soviet Physics JETP 18 (1964) 187.

[19] B. Rossi, High Energy Particles (Prentice-Hill, Inc., Englewood Cliffs, NJ, 1952) ch. 5.

[20] A.M. Hillas, Proc. Cosmic Ray Workshop, University of Utah, ed., T.K. Gaisser, Bartol Research Foundation of the Franklin Inst., Univ. of Delaware, Newark, DE (1983) 16.

[21] A.M. Hillas, Proc. 16th Int. Conf. Cosmic Rays, Kyoto, Japan, 6 (1979) 13.

[22] J. Linsley, Proc. 18th Int. Conf. Cosmic Rays, Bangalore, India, 12 (1983) 135.

[23] T.K. Gaisser, R.J. Protheroe, K.E. Turver, T.J.L. McComb, Rev. Mod. Phys. 50 (1978) 859.

[24] R.P. Feynman, Phys. Rev. Lett. 23 (1969) 1415.

[25] Handbook of Chemistry and Physics, 54th Edition (CRC Press, Cleveland, OH, 1973–74) F190.

[26] K. Greisen, Phys. Rev. Lett. 16 (1966) 748.

Nuclear Instruments and Methods in Physics Research A240 (1985) 429–438
North-Holland, Amsterdam

THE EFFICIENCY OF LEAD SHIELDING FOR BACKGROUND REDUCTION IN UNDERGROUND NEUTRINO EXPERIMENTS

L.S. PEAK and A.M. BAKICH

Falkiner Nuclear Department, School of Physics, University of Sydney, NSW 2006, Australia

Received 7 February 1985

Underground gamma ray fluxes have been measured at a depth of 1230 m, for various thicknesses of lead shielding, in the energy range 0.5–6.0 MeV. From the results it is possible to isolate and examine both the external and internal components of the response of the 10 cm cubical NaI crystal.

Future plans of the Sydney Solar Neutrino Group to extend these measurements with a much larger Cherenkov system are discussed.

1. Introduction

For over a decade now there has been a discrepancy between the number of neutrinos observed to come from the sun, and the number predicted by the standard model of the heating of the interior of the sun. The main experiment involved in such a measurement has been that of Davis [1] in the Homestake mine of South Dakota; whilst the major theoretical contributions have been dominated by the work of Bahcall [2]. Far from being resolved, this discrepancy has in fact grown to something like a factor of 4 as the uncertainties in both experiment and theory have become better understood; and this dearth of observed neutrino flux constitutes the greatest challenge to our conventional understanding of the energy generation mechanism for stars.

There is therefore strong incentive to remeasure this flux using a different technique to that of Davis, and the Sydney neutrino group has for some years been considering the feasibility of constructing a solar neutrino detector in Australia. The proposed method involves the scattering of neutrinos from electron targets in 100 t of pure water, and the subsequent detection of these electrons by means of their emitted Cherenkov radiation. The advantages of such a technique are at least fourfold, and can be listed as follows:

(a) There is some directionality involved, allowing the possibility of correlating the observed events with the motion of the sun.

(b) Pure water is cheap and can serve as both target and detector. The purest waters can have uranium concentrations as low as 10^{-10}–10^{-11} g g^{-1}.

(c) There is greater insensitivity to neutrino type compared with inverse beta reactions. Thus, there is greater immunity to any possible oscillation process between the different species of neutrinos.

(d) Cherenkov detection systems such as this will be insensitive to low energy alpha activity, and hence be unaffected by the whole class of background events involving radioactive decay to alphas.

There are, however, disadvantages which should be listed as well:

(1) The number of photons emitted for any event is extremely low, requiring high surface coverage and efficiency for the photon detectors.

(2) There is no characteristic signature defining a neutrino event. Any incident neutral particle capable of knocking on an electron (such as a Compton scatter) will appear as a neutrino candidate. Moreover, because of the possibility of beta decay from radioactive contamination, one is forced to have a high threshold (greater than 6–7 MeV) for this electron energy. Thus one is restricted to consideration of only the high energy neutrinos resulting from the decay of boron in the solar cycle.

(3) The cross-section, and hence rate, for neutrino electron scattering is extremely low (about 25 events per ton per year with electron energy in excess of 6 MeV) requiring large detectors running for a long time with extremely low background. This poses stringent requirements for stability of equipment and shielding against background. There is a constant and unavoidable background, no matter what the depth of the experiment. This is due to uranium and thorium associated decays in the surrounding ore body giving rise to gamma rays and neutrons. Spontaneous fission of uranium is capable of giving gammas with energy considerably in excess of 14 MeV (the maximum energy of the boron neutrinos), thus posing a real problem for any direct detection experiment such as ours.

0168-9002/85/$03.30
(North-Holland Physics Publishing Division)